Available online at www.sciencedirect.com

SciVerse ScienceDirect

Ceramics International 39 (2013) 1651–1658

CERAMICS INTERNATIONAL

www.elsevier.com/locate/ceramint

Fabrication and characterization of nanocrystalline Mg-substituted fluorapatite by high energy ball milling

M. Kheradmandfard*, M.H. Fathi

Biomaterials Group, Department of Materials Engineering, Isfahan University of Technology, Isfahan, 8415683111, Iran

Received 26 June 2012; received in revised form 3 August 2012; accepted 3 August 2012
Available online 11 August 2012

Abstract

The aim of this work was preparation and characterization of Mg-substituted nanostructured FA powders. Mg-substituted nanostructured FA powders were synthesized with a chemical composition of $Ca_{10-x}Mg_x(PO_4)_6F_2$, with $x=0$, 0.5, 1, 1.5 and 2 by mechanical alloying method. Successful substitution of Ca^{2+} with Mg ions in the fluorapatite lattice was investigated using X-ray diffraction (XRD), scanning electron microscopy (SEM), transmission electron microscopy (TEM), and Fourier transform infrared spectroscopy (FTIR). The results showed that after 12 h of milling, pure nanocrystalline Mg-substituted FA powders with different Mg contents were synthesized. The incorporation of Mg ions into the fluorapatite caused the decrease of the lattice parameters. With increasing Mg content, the crystallinity of powder decreased while the degree of agglomeration of powder increased. SEM and TEM analysis showed that the powder was agglomerated and composed of nanocrystalline particles with the average particle size of less than 100 nm.

Keywords: A. Milling; B. X-ray methods; D. Apatite; Nanostructures

1. Introduction

Because of its good biocompatibility, bioactivity and osteoconductivity with human body constituents, Hydroxyapatite ($Ca_{10}(PO_4)_6(OH)_2$, HA) is widely used in the biomedical fields. [1–4]. Despite these optimal properties, poor thermostability and poor mechanical properties of synthetic HA have limited its clinical applications [5–7]. Biological apatites contain various amounts of substitutions (i.e. F^-, CO_3^{-2}, Na^+, Mg^{+2}, Zn^{+2}) [8,9]. Recently, attention has been given to the modification of properties of apatites, such as bioactivity, biocompatibility, and solubility with ionic substitutions. Fluorine-substituted HA ($Ca_{10}(PO_4)_6(OH)_xF_{2-x}$, FHA) and fluorapatite ($Ca_{10}(PO_4)_6F_2$, FA) have low solubility, good biocompatibility, high thermal and chemical stability [10,11]. These make them very good alternative potential candidates to be used in dental implants and bone repair. Fluorine replacement can favor the crystallization of calcium phosphate, improve thermal stability and decrease the mineral dissolution [5,12,13].

Magnesium (Mg) is one of the most important cationic substitutions for calcium in biological apatites. Dentin, enamel and bone contain 1.23, 0.44, and 0.72 wt% of Mg, respectively. Mg-substituted HA ceramics have been suggested for use in orthopedic and dental applications [9]. The formation and attachment of biomimetic Ca–P coatings in simulated body fluid (SBF) solution were strongly related to Mg^{2+} content and Mg-substitution improves the bioactivity of apatite in SBF [14,15].

Keeping the above points in view, Mg^{2+} substituted FA bioceramics are expected to have better biocompatibility and biological properties than pure FA [15,16].

Mechanical alloying (MA) is an effective way of preparing nanocrystalline or nanostructured materials, such as ceramics, composites and intermetallic compounds. MA method offers a simple, powerful, and economical tool for fabrication of several advanced materials [17–19].

The aim of this work is to prepare and characterize FA nanopowders with different Mg contents via mechanical alloys.

*Corresponding author. Tel.: +98 913 1290434; fax: +98 311 3912752.
E-mail address: mkh_fard@yahoo.com (M. Kheradmandfard).

0272-8842/$ - see front matter © 2012 Elsevier Ltd and Techna Group S.r.l. All rights reserved.
http://dx.doi.org/10.1016/j.ceramint.2012.08.007

2. Materials and methods

2.1. Powder preparation

A mixture of phosphorous pentoxide (P_2O_5), calcium hydroxide ($Ca(OH)_2$), magnesium hydroxide ($Mg(OH)_2$), and calcium fluoride (CaF_2 powders (all p.a., Merck)) were mechanically activated, using a high energy planetary ball mill with 125 ml zirconia vial and four 20 mm diameter zirconia balls at ambient temperature. Mechanical alloying was performed using ball/powder mass ratio of 25:1 and rotation speed of 250 rpm. Ball milling was executed for 2, 4, 8, 12 and 15 h. The designated degree of Ca^{2+} substitution by Mg^{2+} in the mixture, was indicated by the x value in the general formula of FA ($Ca_{10-x}Mg_x(PO_4)_6F_2$), where x gets the value of 0, 0.5, 1, 1.5, and 2. The subsequent obtained powders were named FAM0, FAM5, FAM10, FAM15 and FAM20, respectively.

2.2. Powder characterization

A Philips diffractometer (40 kV) with Cu Kα radiation ($\lambda = 0.15406$ nm) was used to investigate the structural changes and phase analysis of the powders during mechanical alloying. All X-ray diffraction (XRD) tests were performed in the 2θ range of 15–65° (step size 0.03° and time per step 1 s). The crystallite size and internal strain of prepared powders was determined using XRD patterns and Williamson–Hall approach [20]

$$B\cos\theta = 0.9\lambda/D + \varepsilon\sin\theta \quad (1)$$

where B is the full-width at half maximum intensity, λ is the wavelength of the X-ray used ($\lambda = 0.154056$ nm), D is the average crystallite size (nm), θ is the Bragg angle and ε is the average strain.

The fraction of crystalline phase (X_c) in the obtained powders could be evaluated by the following equation [21]:

$$X_c = 1 - \frac{V_{112/300}}{I_{300}} \quad (2)$$

where I_{300} is the intensity of (300) diffraction peak and $V_{112/300}$ is the intensity of the hollow between (112) and (300) diffraction peaks of the produced powders. The functional groups of samples were analyzed and identified with Fourier transform infrared spectroscopy (FTIR, Bomem, MB100) in a mid-IR spectrum range in the range of 400–4000 cm^{-1}. The morphology and agglomerates size distributions of the obtained powders were investigated by scanning electron microscopy (SEM, Phillips XL 30: Eindhoven, The Netherlands). Energy dispersive X-ray spectrometer (EDS) analysis and elemental mapping were

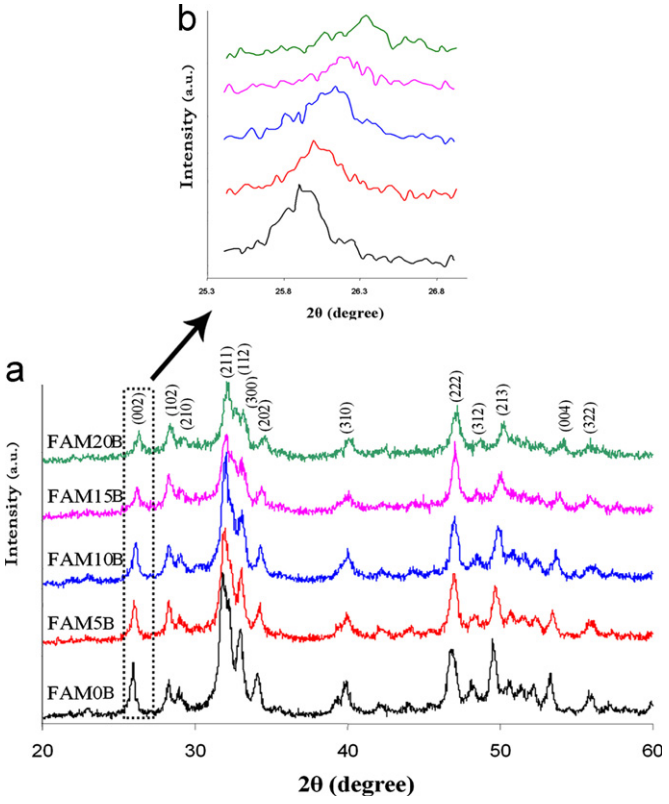

Fig. 2. XRD patterns of obtained FAM0, FAM5, FAM10, FAM15 and FAM20 after ball milling for 12 h.

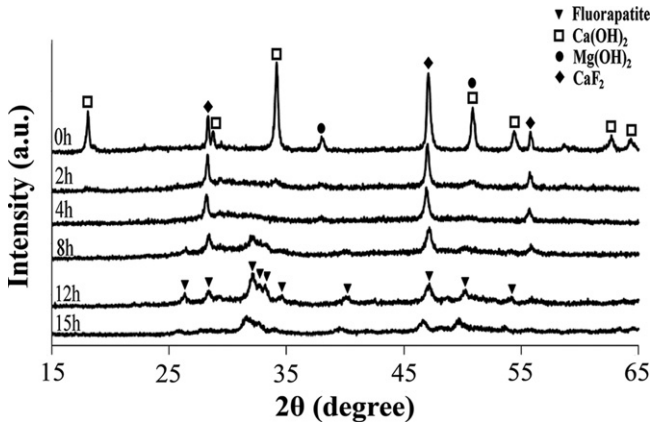

Fig. 1. XRD patterns of starting materials before and after ball milling versus different milling times.

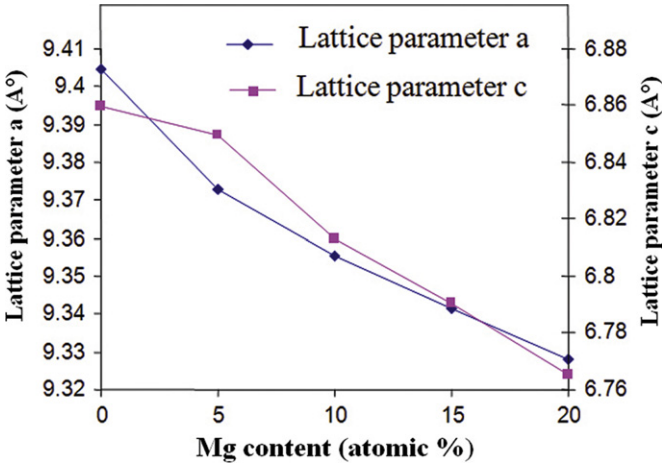

Fig. 3. The lattice parameters of obtained powders versus different Mg contents.

performed with a SERON AIS 2300C SEM equipped with an EDS analyzer, worked at 25 kV. The atomic concentration of Mg in the obtained powders were quantified through inductively coupled plasma optical emission spectrometry (ICP-OES) (OPTIMA 7300DV). The morphology and particle size of the powders were checked using transmission electron microscopy (TEM) working at 200 kV.

3. Results and discussion

3.1. Phase structure analysis

Fig. 1 shows the XRD patterns of FAM20 powder mixture before and after ball milling with different ball milling durations. The pattern of initial powder mixture (at 0 h) includes the sharp characteristic peaks of $Ca(OH)_2$, $Mg(OH)_2$, and CaF_2. The characteristic peaks of P_2O_5 could not be detected because of high hydrophilic of P_2O_5 which causes the formation of phosphoric acid, immediately [22]. With increasing the ball milling time, the intensity of $Ca(OH)_2$, $Mg(OH)_2$ and CaF_2 diffraction peaks decreased and their width increased progressively. After 4 h of ball milling, the peaks of $Ca(OH)_2$ disappeared in pattern while those of $Mg(OH)_2$ and CaF_2 were still observed. After 8 h of ball milling, apatite phase was noticed by the appearance of broad and weak characteristic peaks around 31.7–33.7°. By increasing the ball milling duration up to 12 h, the crystalline apatite phase was formed while FA peaks were shifted toward higher angles in comparison with standard card of FA (#15–0876). This happened because of dissolution of smaller Mg ionic radius than that of Ca^{2+} ions into the FA lattice [23,24]. After MA for 15 h the FA peaks shifted slightly to the lower angles suggesting that Mg atoms are rejected

Table 1
Crystallite size, lattice strain, and crystallinity of obtained FA powders.

Sample	Crystallite size (nm)	Lattice strain (%)	Crystallinity, X_c (%)
FAM0	60	0.96	44.14
FAM5	42	0.74	41.87
FAM10	34	0.65	30.56
FAM15	46	0.68	28.87
FAM20	69	0.95	27.31

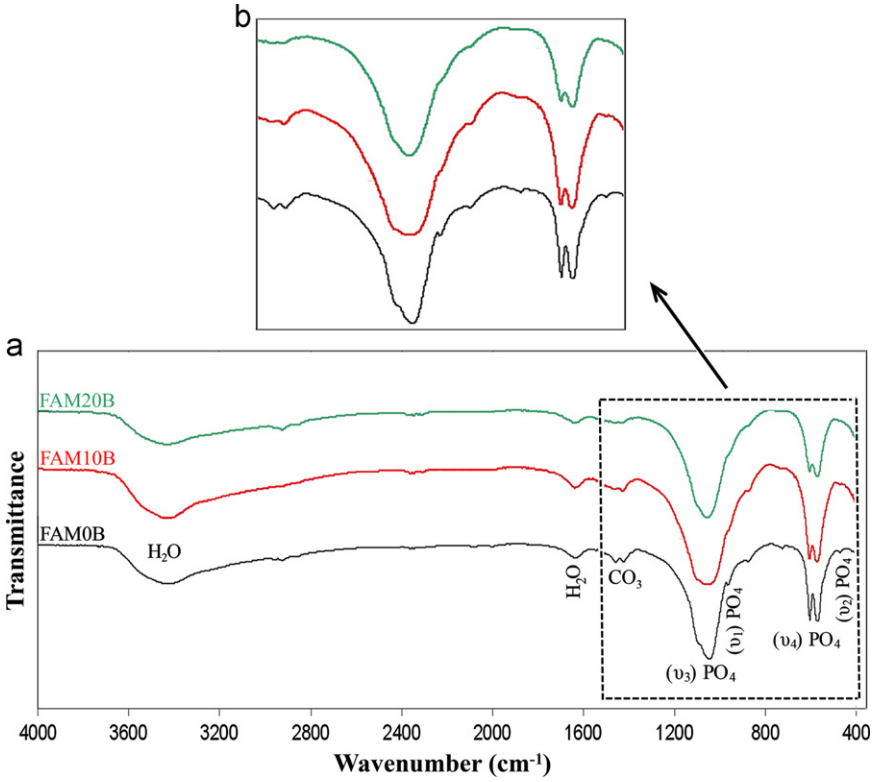

Fig. 4. FTIR spectra of obtained FA powders with different Mg contents.

from FA lattice. In fact, the internal energy of the Mg-substituted FA mixture during milling increases due to the formation of a supersaturated solid solution and a high density of dislocations. Therefore, system tends to reduce its internal energy by formation of a cell structure and then high angle grain boundaries. The Gibbs free energy (G) will be further decreased by diffusion of Mg atoms from grain internal toward the grain boundaries and as a result, Mg-substituted FA supersaturated solid solution decomposes. Similar behavior was reported in the case of the MA behavior of Al–Zn alloy [25].

XRD patterns of obtained FAM0, FAM5, FAM10, FAM15, and FAM20 powders subjected to ball milling for 12 h are shown in Fig. 2. No other peaks except for characteristic FA peaks were observed. Characteristic peaks gradually shifted to the right-hand side with the rise of Mg ions incorporated within the FA lattice (Fig. 2b).

Since Mg ionic radius (0.065 nm) is smaller than that of Ca^{2+} ions (0.099 nm), the ion substitution of calcium by smaller Mg ions resulted in a contraction of the cell parameters of FA [23,24]. Fig. 3 shows the change in FA lattice parameters as a function of Mg content. It can be seen that by increasing Mg content, the lattice parameters of obtained powders decreased which confirm the substitution of Ca^{2+} with Mg ions in the FA lattice.

With increasing Mg content, the crystallinity of the FA phase gradually decreased as revealed by increased broadening and decreased intensity of their XRD peaks (Fig. 2b) which is in agreement with previous works [9,23,24]. However, this result is in contrast with the findings of our previous study [26], which showed the crystallinity of FA, fabricated by sol–gel method, almost remains unchanged with increasing Mg substitutions into the FA lattice. This different behavior can be related to the differences in methods of fabrication.

The amounts of crystallite size, lattice strain, and crystallinity of prepared FA powders with different Mg content are shown in Table 1. The crystallite size of obtained powders is in the range of 34–69 nm. The gradual decrease of crystallinity suggests increasing Mg substitution in the FA lattice with increasing Mg content [24]. Similar results were reported in the case of HA-containing Mg ions [9].

3.2. FTIR evaluation

Fig. 4 shows FTIR spectra of FAM0, FAM10, and FAM20 samples. The IR spectra of each of the prepared powders are characteristic of apatite compounds. The band at 963 cm^{-1} was attributed to υ_1 vibration peak of PO_4^{3-} [27]. The 472 cm^{-1} band was derived from the υ_2 phosphate mode [28]. As a major peak of phosphate group, the υ_3 vibration peak was observed in the region between 1000 and 1100 cm^{-1}. The absorption peaks located at 577 and 603 cm^{-1}, were assigned to the υ_4 vibration mode of PO_4^{3-} [29]. The weak absorption bands at 1425 cm^{-1}, 1459 cm^{-1}, and 877 cm^{-1} were derived from the υ_3 and the υ_2 vibration of CO_3^{-2} group, respectively [22]. The wide absorption band observed at 3100–3400 cm^{-1} is attributed to lattice H_2O [22,27,28].

The absorption band at 1640 cm^{-1} was attributed to H_2O bending mode [28]. With an increase in the Mg content, the band intensity and band resolution corresponding to PO_4^{-3} and CO_3^{-2} vibration modes decreased (Fig. 4b), suggesting that Mg was substituted in the FA lattice. In other words, with increasing Mg content, the lattice disorder was increased due to Mg substitution in

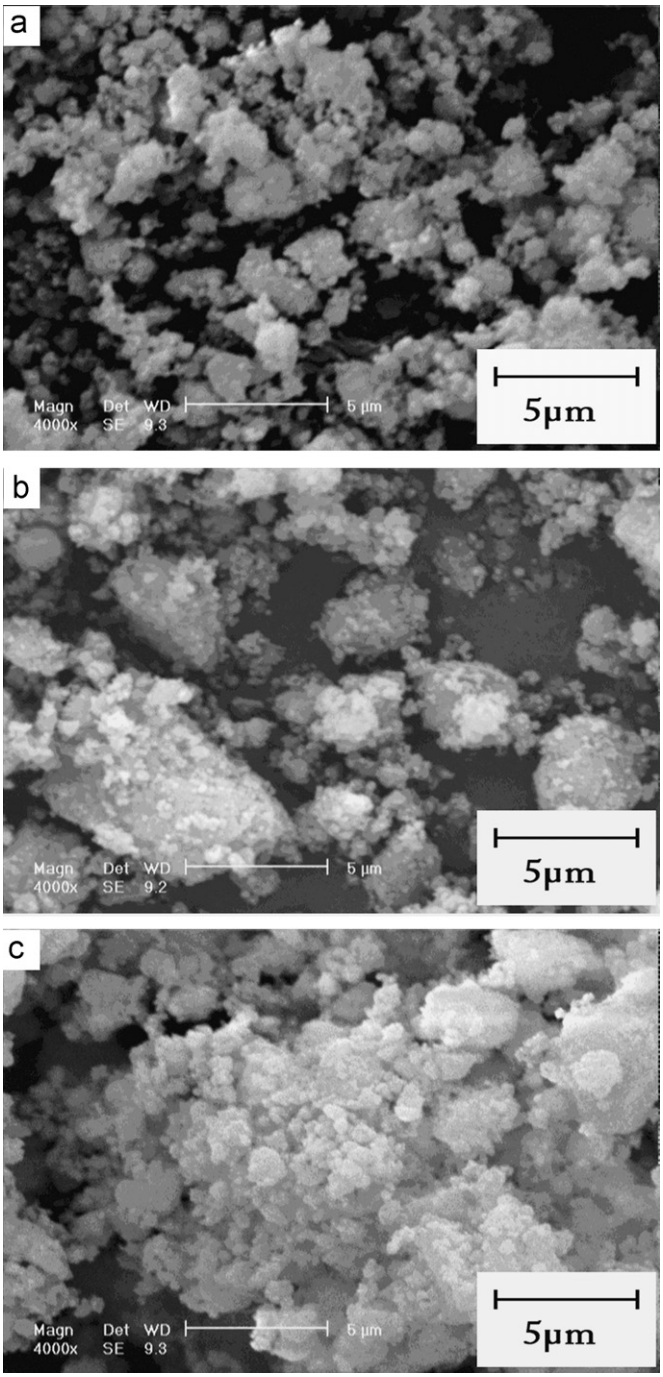

Fig. 5. SEM micrograph of (a) FAM0, (b) FAM10, and (c) FAM20 Mg-doped FA powders.

FA lattice [9]. This result is also in agreement with the XRD results.

3.3. SEM, EDS and ICP analysis

Fig. 5 shows the morphology of obtained FA powders with different Mg contents. The morphology of powders indicates that each of them is composed of agglomerates with irregular shape and dimension distributions. It can be seen that by increasing Mg content, the degree of agglomeration of powders increased [24]. High magnification microstructures of the FAM10 and FAM20 powders (Fig. 6) indicate that the agglomerated particles in Fig. 5 are composed of very fine particles. It is also confirmed that, with increasing Mg substitutions into the FA lattice, the crystallinity of powder decreased while the degree of agglomeration of powder increased. The results of measurements of elemental composition and elemental mapping of FAM20 powder by EDS are presented in Fig. 7. The elemental maps show homogenous distribution of elements in the structure. However, the dots densities of elemental maps are not the same. It is well known that the dots density depends on the concentration and atomic number of the elements [30]. As it can be seen from the elemental composition, the concentrations of Mg and F ions are much lower than those of other elements (Ca and P) in the obtained powder. Furthermore, with respect to the Ca and P ions, Mg and F ions have lower atomic numbers. Therefore, it is confirmed that the dots density of Mg and F ions must be much lower than that of Ca and P ions. It should be noted that the effect of low atomic number of F ions on the dots density is more severe than that of Mg ions.

Fig. 8 shows the chemical analysis of the obtained Mg–FA nanopowders. As can be seen, with increasing x, Mg concentration of powders was increased. Furthermore, the measured Mg contents are in good agreement with the designated Mg contents of powders.

3.4. TEM analysis

The morphological shape and size of FAM10 and FAM20 powders obtained from TEM are shown in Fig. 9. The TEM images indicate the nanocrystalline nature of materials. The TEM images reveal that powders are composed of nanocrystalline particles with the average particle size of less than 100 nm. This is in agreement with the crystallite size of Mg–FA powders calculated using XRD data.

Nanocrystalline bioceramics have attracted much interest, due to their unique and superior properties that are often different from their bulk materials counterpart. These materials can possess superior biological properties [31]. The obtained powders had a crystallite size in the range of nano scale.

The essential requirement for biomaterials to bond to living bone is formation of the bone-like apatite (carbonate-containing hydroxyapatite) layer on their surface in

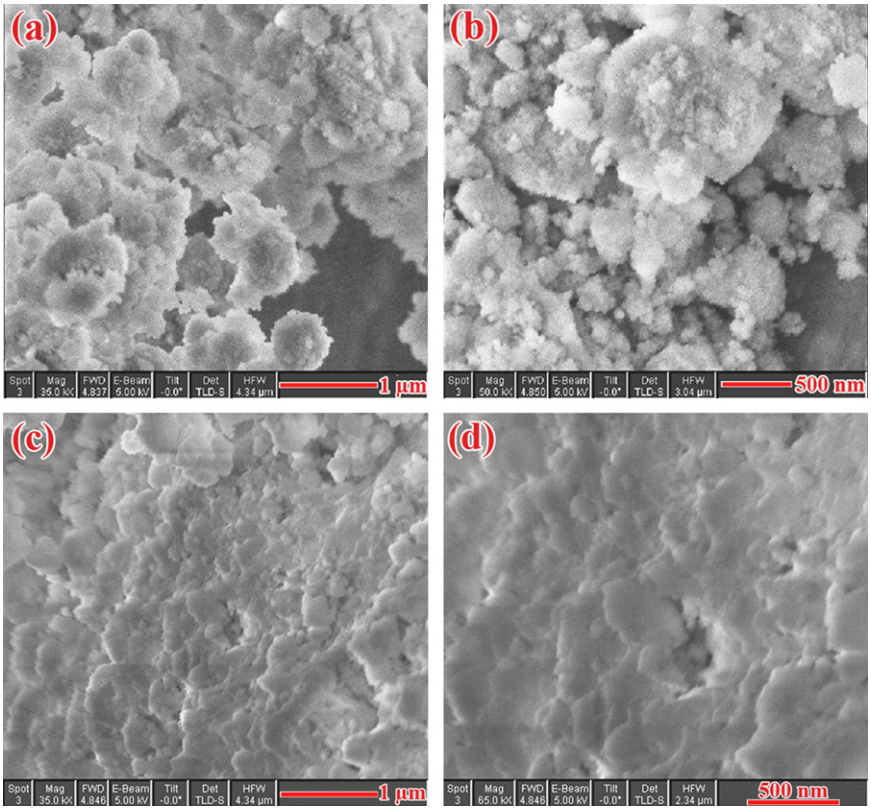

Fig. 6. SEM micrographs of (a, b) FAM10 and (c, d) FAM20 powders in high magnifications.

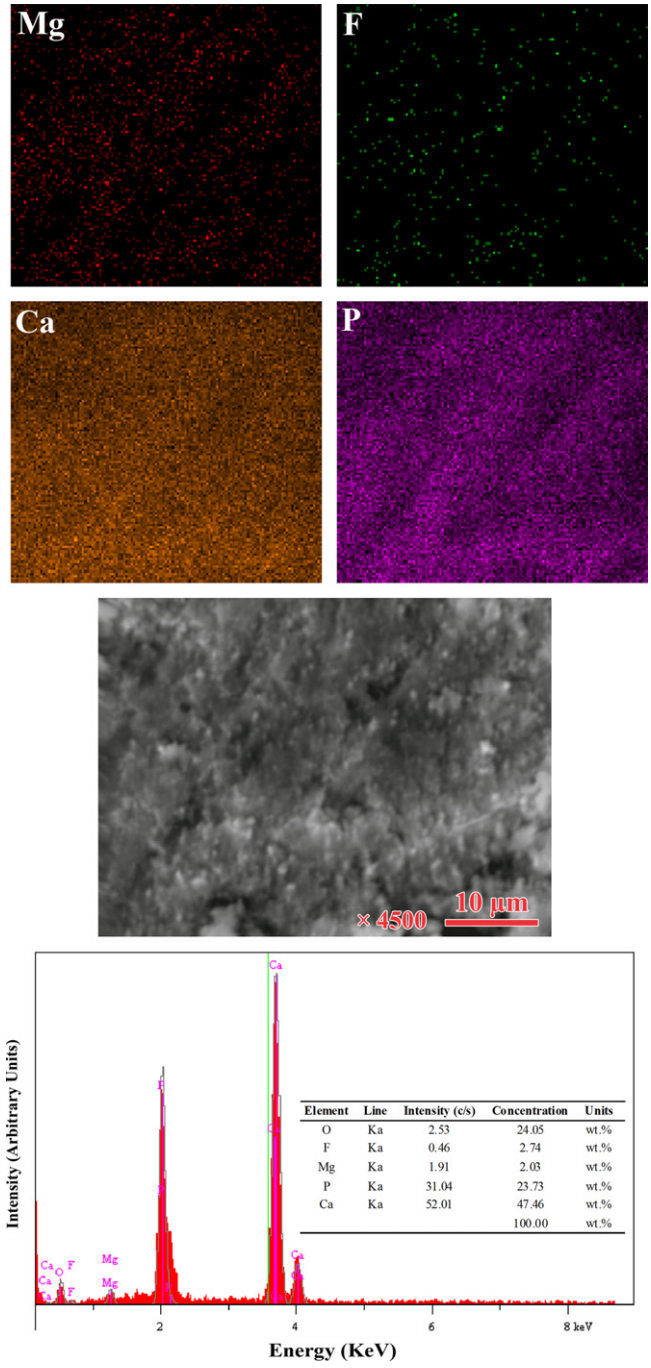

Fig. 7. Elemental composition and elemental mapping of FAM20 powder by EDS.

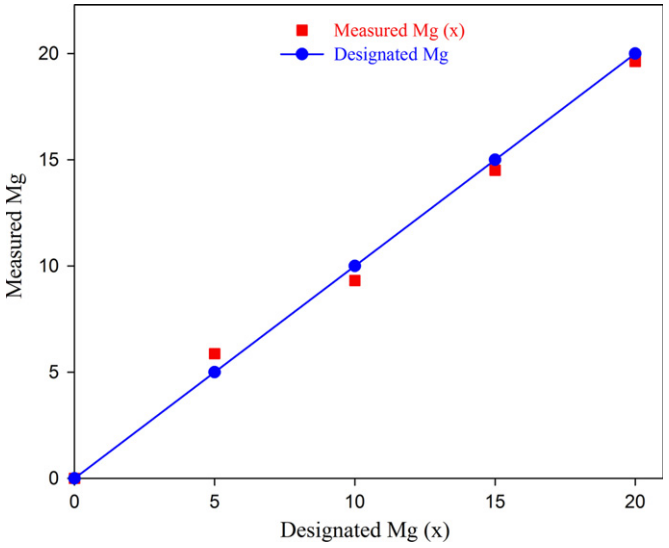

Fig. 8. Changes in measured Mg concentration versus different designated Mg (x).

the body within a physiological environment. Solubility of apatites is one of most important factors for their application; a greater solubility of apatite would provide a better bioactivity. Dissolution of apatite results in redistribution of Ca^{2+} and PO_4^{3-} ions which may be used by surrounding tissues in the manufacture of new bone-like apatite. In fact, the increase in concentrations of Ca^{2+} and PO_4^{3-} ions resulted in the increase of local supersaturation, which is beneficial to nucleation and growth of the new apatite crystals [32,33]. However, if apatite acts as a coating on the implant surface, high dissolution could deteriorate the bonding between the implant surface and newly grown bone, and as a result, the function of the coating will be degraded. Therefore, it is important for bioactive apatite coating to have a reasonable solubility [34]. The in vitro dissolution characteristics of apatites are controlled by the properties of materials such as chemical composition, crystallinity, method of preparation, crystal particle size and the extent of ionic substitutions into the apatite lattice. Ionic substitutions increase the lattice disorder and tailor the dissolution properties of the material in solution. The degree of crystallinity also influences the dissolution behavior of apatites. Apatites with high degree of crystallinity tend to be very insoluble, while apatites with low degree of crystallinity have higher relative solubilities [35].

Controlling the amount of Mg^{2+} substitution in FA is an appropriate way to not only take advantage of the desirable properties of Mg, but also tailor the crystallinity, solubility, bioactivity and physicochemical properties of the synthesized crystals.

4. Conclusions

Pure nanocrystalline Mg-substituted FA powders with different Mg contents were fabricated via mechanical activation. Substitution of Ca^{2+} with Mg ions in the FA lattice successfully occurred. The incorporation of Mg ions into the FA lattice caused the decrease of the lattice parameters and crystallinity. The obtained powder was agglomerated and composed of nanocrystalline particles with the average particle size of less than 100 nm. The results showed that after 12 h of milling, pure nanocrystalline Mg-substituted FA powders with different Mg contents were synthesized. Controlling the amount of Mg^{2+} substitution in FA is an appropriate way to not only take advantage of the desirable

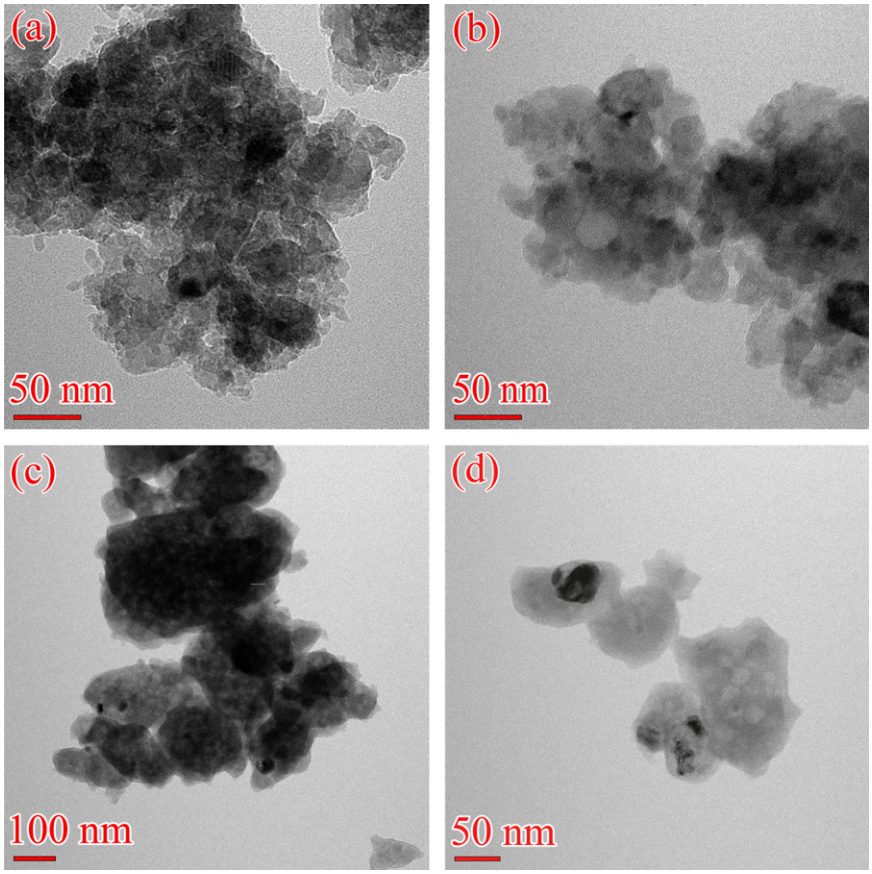

Fig. 9. TEM micrographs of (a, b) FAM10 and (c, d) FAM20 powders.

properties of Mg, but also tailor the crystallinity, solubility, bioactivity and physicochemical properties of the synthesized crystals.

Acknowledgment

The authors are grateful to the Isfahan University of Technology for supporting the present research.

References

[1] H. Zhang, B.W. Darvell, Constitution and morphology of hydroxyapatite whiskers prepared using amine additives, Journal of the European Ceramic Society 30 (2010) 2041–2048.
[2] I. Cacciotti, A. Bianco, M. Lombardi, L. Montanaro, Mg-substituted hydroxyapatite nanopowders: Synthesis, thermal stability and sintering behaviour, Journal of the European Ceramic Society 29 (2009) 2969–2978.
[3] F. Chen, Z.C. Wang, C.J. Lin, Preparation and characterization of nano-sized hydroxyapatite particles and hydroxyapatite/chitosan nano-composite for use in biomedical materials, Materials Letters 57 (2002) 858–861.
[4] M.H. Fathi, A. Hanifi, Evaluation and characterization of nanostructure hydroxyapatite powder prepared by simple sol–gel method, Materials Letters 61 (2007) 3978–3983.
[5] S.J. Kim, H.G. Bang, J.H. Song, S.Y. Park, Effect of fluoride additive on the mechanical properties of hydroxyapatite/alumina composites, Ceramics International 35 (2009) 1647–1650.
[6] Y. Chen, X. Miao, Effect of fluorine addition on the corrosion resistance of hydroxyapatite ceramics, Ceramics International 30 (2004) 1961–1965.
[7] W. Que, K.A. Khor, J.L. Xu, L.G. Yu, Hydroxyapatite/titania nanocomposites derived by combining high-energy ball milling with spark plasma sintering processes, Journal of the European Ceramic Society 28 (2008) 3083–3090.
[8] A. Bianco, I. Cacciotti, M. Lombardi, L. Montanaro, Si-substituted hydroxyapatite nanopowders: Synthesis, thermal stability and sinterability, Materials Research Bulletin 44 (2009) 345–354.
[9] W.L. Suchanek, K. Byrappa, P. Shuk, R.E. Riman, V.F. Janas, K.S. TenHuisen, Preparation of magnesium-substituted hydroxyapatite powders by the mechanochemical–hydrothermal method, Biomaterials 25 (2004) 4647–4657.
[10] A. Bianco, I. Cacciotti, M. Lombardi, L. Montanaro, E. Bemporad, M. Sebastiani, F-substituted hydroxyapatite nanopowders: Thermal stability, sintering behaviour and mechanical properties, Ceramics International 36 (2010) 313–322.
[11] B.I. Bogdanov, P.S. Pashev, J.H. Hristov, I.G. Markovska, Bioactive fluorapatite-containing glass ceramics, Ceramics International 35 (2009) 1651–1655.
[12] K. Cheng, G. Han, W. Weng, H. Qu, P. Du, G. Shen, J. Yang, J.M.F. Ferreira, Sol–gel derived fluoridated hydroxyapatite films, Materials Research Bulletin 38 (2003) 89–97.
[13] S. Miao, W. Weng, K. Cheng, P. Du, G. Shen, G. Han, S. Zhang, Sol–gel preparation of Zn-doped fluoridated hydroxyapatite films, Surface and Coatings Technology 198 (2005) 223–226.
[14] F. Barrere, C.A. van Blitterswijk, K. de Groot, P. Layrolle, Nucleation of biomimetic Ca–P coatings on Ti_6Al_4V from a SBF × 5 solution: Influence of magnesium, Biomaterials 23 (2002) 2211–2220.

[15] M. Kheradmandfard, M.H. Fathi, M. Ahangarian, E. Mohammadi Zahrani, In vitro bioactivity evaluation of magnesium-substituted fluorapatite nanopowders, Ceramics International 38 (2012) 169–175.
[16] Y. Cai, S. Zhang, X. Zeng, Y. Wang, M. Qian, W. Weng, Improvement of bioactivity with magnesium and fluorine ions incorporated hydroxyapatite coatings via sol–gel deposition on Ti_6Al_4V alloys, Thin Solid Films 517 (2009) 5347–5351.
[17] M. Ali, P. Basu, Mechanochemical synthesis of nano-structured TiC from TiO_2 powders, Journal of Alloys and Compounds 500 (2010) 220–223.
[18] Z.H. Yang, Y. Zhou, D.C. Jia, Q.C. Meng, Microstructures and properties of $SiB_{0.5}C_{1.5}N_{0.5}$ ceramics consolidated by mechanical alloying and hot pressing, Materials Science and Engineering A 489 (2008) 187–192.
[19] H. Shi, D. Guo, Y. Ouyang, Structural evolution of mechanically alloyed nanocrystalline FeAl intermetallics, Journal of Alloys and Compounds 455 (2008) 207–209.
[20] G.K. Williamson, W.H. Hall, X-ray line broadening from filed aluminium and wolfram, Acta Metallurgica 1 (1953) 22–31.
[21] E. Landi, A. Tampieri, G. Celotti, S. Sprio, Densification behaviour and mechanisms of synthetic hydroxyapatites, Journal of the European Ceramic Society 20 (2000) 2377–2387.
[22] M.H. Fathi, E. Mohammadi Zahrani, Fabrication and characterization of fluoridated hydroxyapatite nanopowders via mechanical alloying, Journal of Alloys and Compounds 475 (2009) 408–414.
[23] Z. Yang, Y. Jiang, L.X. Yu, B. Wen, F. Li, S. Sun, T. Hou, Preparation and characterization of magnesium doped hydroxyapatite–gelatin nanocomposite, Journal of Materials Chemistry 15 (2005) 1807–1811.
[24] M. Hidouri, K. Bouzouita, F. Kooli, I. Khattech, Thermal behaviour of magnesium-containing fluorapatite, Materials Chemistry and Physics 80 (2003) 496–505.
[25] M. Tavoosi, M.H. Enayati, F. Karimzadeh, Softening behaviour of nanostructured Al–14 wt% Zn alloy during mechanical alloying, Journal of Alloys and Compounds 464 (2008) 107–110.
[26] M. Kheradmandfard, M.H. Fathi, Preparation and characterization of Mg-doped fluorapatite nanopowders by sol–gel method, Journal of Alloys and Compounds 504 (2010) 141–145.
[27] A. Rapacz-Kmita, C. Paluszkiewicz, A. Slosarczyk, Z. Paszkiewicz, FTIR and XRD investigations on the thermal stability of hydroxyapatite during hot pressing and pressureless sintering processes, Journal of Molecular Structure 653 (2005) 744–747.
[28] Y. Liu, W. Wang, Y. Zhan, C. Zheng, G. Wang, A simple route to hydroxyapatite nanofibers, Materials Letters 56 (2002) 496–501.
[29] R. Murugan, S. Ramakrishna, Aqueous mediated synthesis of bioresorbable nanocrystalline hydroxyapatite, Journal of Crystal Growth 274 (2005) 209–213.
[30] P.J. Goodhew, J. Humphreys, R. Beanland, Electron Microscopy and Analysis, Third ed., Taylor and Francis, 2001, pp. 180–200.
[31] T.J. Webster, R.W. Siegel, R. Bizios, Osteoblast adhesion on nanophase ceramics, Biomaterials 20 (1999) 1221–1227.
[32] Q. Zhang, J. Chen, J. Feng, Y. Cao, C. Deng, X. Zhang, Dissolution and mineralization behaviors of HA coatings, Biomaterials 24 (2003) 4741–4748.
[33] H.C. Gledhill, I.G. Turner, C. Doyle, In vitro dissolution behaviour of two morphologically different thermally sprayed hydroxyapatite coatings, Biomaterials 22 (2001) 695–700.
[34] K. Cheng, G. Shen, W. Weng, G. Han, J.M.F. Ferreira, J. Yang, Synthesis of hydroxyapatite/fluoroapatite solid solution by a sol–gel method, Materials Letters 51 (2001) 37–41.
[35] M.T. Fulmer, I.C. Ison, C.R. Hankermayer, B.R. Constantz, J. Ross, Measurements of the solubilities and dissolution rates of several hydroxyapatites, Biomaterials 23 (2002) 751–755.